

Cite this: *J. Mater. Chem. A*, 2018, 6, 24285

Primary amine modulated synthesis of two-dimensional porous nanocarbons with tunable ultramicropores†

Lu-Hua Zhang, Wen-Cui Li, Lei Tang, Quan-Gao Wang, Qing-Tao Hu, Yu Zhang and An-Hui Lu *

Porous carbons with a two-dimensional (2D) morphology and narrow micropore size distribution can significantly enhance molecular separation efficiency. The precise control of micropore size is desirable; however it remains a big challenge as most reported carbon materials usually have non-uniform distribution of micropores. Herein, a group of 2D porous nanocarbons with single-sized ultramicropores was synthesized by relying on the polybenzoxazine chemistry using primary amines with various aliphatic chain lengths as the modulator. The unimodality of the micropore size of 2D porous nanocarbons depends on the length of aliphatic chains in the amine moieties. By pyrolysis of short chain amine induced polybenzoxazines, the produced 2D porous nanocarbons mainly consist of sp^2 carbon, which leads to the stacking of crystallites in a nearly parallel orientation, resulting in the formation of unimodal ultramicropores. When evaluated as an adsorbent for CO_2 capture, the 2D porous nanocarbons, with a high adsorption capacity (5.2 mmol g^{-1}), an excellent selectivity (192) and fast sorption kinetics under ambient conditions, are complemented by the fact that equilibrium uptakes can be achieved in dynamic flow situations.

Received 2nd October 2018
Accepted 4th November 2018

DOI: 10.1039/c8ta09545k

rsc.li/materials-a

Introduction

Owing to larger accessible geometrical surfaces and shorter diffusion paths compared to their bulk counterparts, two-dimensional (2D) nanostructured materials with extended lateral dimensions and nanometer thickness show advantages in many diffusion-controlled systems such as gas adsorption and separation, electrochemical energy storage, and catalysis. 2D nanocarbons generally have advanced properties, such as high surface area, good chemical and thermal stabilities and excellent moisture resistance, which led to increased interest in developing innovative synthesis routes of 2D nanocarbons.^{1–3}

Literature established synthesis routes of 2D nanocarbons fall into two categories: the top-down approach and bottom-up approach. The top-down exfoliation approach relies on the disintegration of bulk-layered crystalline mother materials, while the bottom-up strategies produce 2D structures through precise atomic, ionic and molecular self-assembly.^{4–6} A significant advantage of the bottom-up synthesis is that the molecular structure of self-assembled organic substances, namely carbon precursors, can be customized through the selection of different monomers. However, controlled assembly leading to

anisotropic 2D structures poses a conceptual challenge in the field of materials research, because the existence of a high proportion of lateral surfaces means a high free energy in the synthesis system.^{7–10} Thus, most of the 2D carbons were prepared by employing graphene oxides,^{11–19} metal salts,^{20–24} MgO ,²⁵ and layered double hydroxides²⁶ as a shape-directing agent. To date, there have been only a few examples of 2D nanocarbon synthesis involving the self-assembly of organic substances without any hard-template.^{27–29} Nevertheless, organic substances usually have lower melting points and can be easily decomposed and deformed during pyrolysis. Furthermore, the restacking and curling of these 2D carbons are always inevitable to minimize surface free energy, preventing full utilization of surface area by blocking the access of guest molecules. Thus, it is hard to retain the desired morphology and pore structures, particularly in regard to nanometer sized dimensions.

Fortunately, our previous studies have demonstrated that polybenzoxazine-based nanocarbon materials such as nanospheres,^{30–32} nanosheets^{11–13} and nanoplates³³ can generally inherit the morphology of the starting polymers that can withstand thermal degradation. Recently, we reported that carbon nanoplates with unimodal ultramicropores can be prepared using thermoregulated phase transition methods for selective natural gas separation and purification.³³ Considering the advantage of excellent morphology-retention and low thermal shrinkage of polybenzoxazine-based carbon materials, we are

State Key Laboratory of Fine Chemicals, School of Chemical Engineering, Dalian University of Technology, Dalian 116024, P. R. China. E-mail: anhuilu@dlut.edu.cn

† Electronic supplementary information (ESI) available: SEM, XPS, elemental analysis, XRD and Raman spectroscopy results. See DOI: 10.1039/c8ta09545k

motivated to investigate how to further precisely tune the micropore size and distribution of such nanocarbons.

The assembled molecular structure of polybenzoxazines is a crucial factor that affects the morphology and porosity evolution of the corresponding carbons during pyrolysis.^{34,35} The Mannich base bridge ($-\text{CH}_2-\text{NR}'-\text{CH}_2-$) is a characteristic of polybenzoxazines, and the Mannich base shows a significant degree of hydrogen bonding with the phenolic OH groups ($-\text{OH}\cdots\text{N}$ intramolecular hydrogen bonding). The strength of hydrogen bonding depends on the basicity and bulkiness of the amines.^{36–38} Thus, different types of amine substituents (R') would have an impact on the thermal degradation of polybenzoxazines, accordingly influencing the microporous structures of their carbon counterparts. Therefore, we decide to investigate the influence of the aliphatic chain length of the primary amine moieties on the micropore structure of the 2D nanocarbons.

Results and discussion

The primary amines used in our research include ethylamine (EA), ethylenediamine (EDA), propylamine (PA), 1,3-diaminopropane (DAP), butylamine (BA), hexylamine (HA), and 1,6-diaminohexane (DAH). The synthesis process generally relied on the thermoregulated phase transition method.³³ Field-emission scanning electron micrographs (SEM) of all the carbon samples show flat and thin 2D structures with micrometer lateral dimensions (approximately $4\ \mu\text{m} \times 1\ \mu\text{m}$), demonstrating that the selected primary amines are applicable for the synthesis of 2D polybenzoxazine-based porous nanocarbons. The average thickness ranges from 48 nm to 60 nm,

depending on the aliphatic chain length of the primary amines under identical synthesis conditions (Fig. 1a–h and S1†). The high transparency of carbon samples, in the transmission electron microscopy (TEM) images, can be clearly observed in some cracked and staggered portions (yellow oval in Fig. 1i), further highlighting their ultrathin nature. Even more remarkable, the oriented multilayer regions consist of several graphene layers, as observed at the edge of representative 2D porous nanocarbons (Fig. 1g–l). Compared to other amorphous carbons characterized by a random orientation and rigid cross-linking of turbostratic nanodomains, the stacking of sp^2 graphene carbon sheets is oriented parallelly in a two-dimensional thin structure.

The nitrogen sorption isotherms of all 2D porous nanocarbon samples are type I, reflecting the microporous characteristic (Fig. 2a). Their surface areas are in the range of $360\text{--}550\ \text{m}^2\ \text{g}^{-1}$ (Table 1). For the primary amine (EA, PA, BA, and HA) modulated 2D polybenzoxazine-based nanocarbons, the corresponding pore size distributions (PSDs) of C-EA, C-PA, C-BA, and C-HA are 5.8, 5.8, 5.8/8.0/11.5, and 5.8/8.0 Å, respectively (Fig. 2b). Clearly, when the aliphatic chain length is larger than three carbons, the pore sizes extend from monomodal to bi- or tri-modal distributions, but the overall pore sizes are still in the micropore range. The majority of the pore sizes are 5.8 Å, while the minority of the pore sizes are 8 Å and 11.5 Å. For the primary diamine (EDA, DAP, and DAH) induced 2D polybenzoxazine-based nanocarbons, the PSDs of C-EDA, C-DAP, C-DAH, are 5.3, 5.8/8.0, and 5.8/8.0/11.5 Å, respectively. By comparing the PSDs of primary amines and diamines, one can speculate that the pore size unimodality of the obtained nanocarbons has a certain dependence on the length of aliphatic chains and the

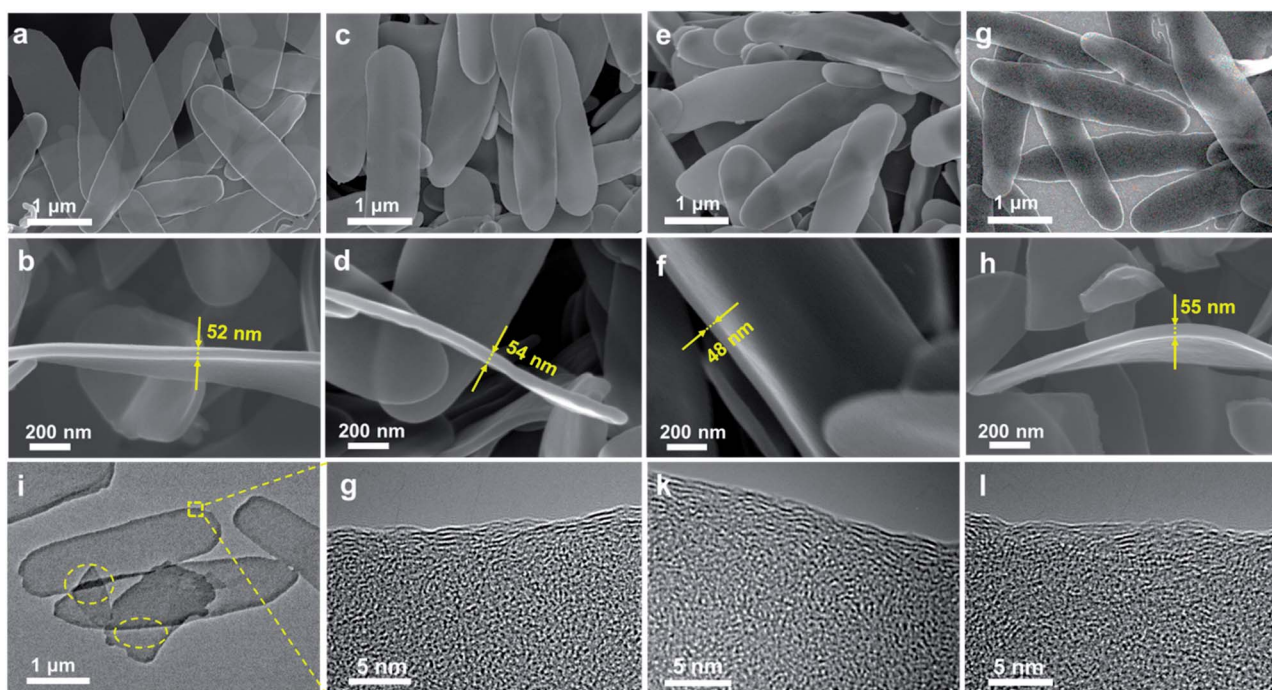


Fig. 1 SEM images of (a and b) C-EDA, (c and d) C-PA, (e and f) C-DAH, and (g and h) C-PA-KC, and TEM images of (i and j) C-PA, (k) C-EDA, and (l) C-DAH. For a given sample, about 10 carbon samples were quantified to obtain the average thickness.

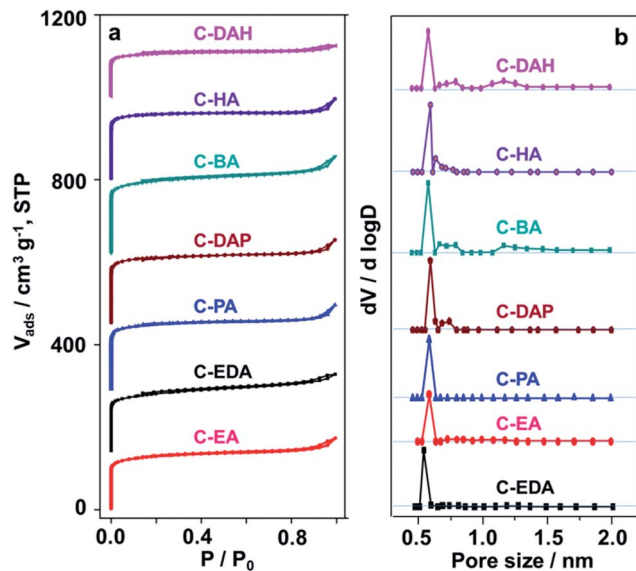


Fig. 2 (a) N_2 adsorption isotherms and (b) the corresponding PSDs of 2D polybenzoxazine-based nanocarbons, the adsorption isotherms of C-EDA, C-PA, C-DAP, C-BA, C-HA, and C-DAH are vertically offset by 140, 290, 450, 620, 800, and 1000 $cm^3 g^{-1}$, STP, respectively.

amine moieties. We can conclude that, when the total number of carbon and nitrogen atoms is less than four, the obtained 2D porous nanocarbons show nice single-sized ultramicropores.

The elemental analysis and X-ray photoelectron spectroscopy (XPS) show a carbon and an oxygen content in 2D nanocarbons of 80–90 wt% and ~10 wt%, respectively (Fig. S2 and Table S1†). C-EA, C-EDA, and C-PA with a single-sized pore system tend to show a high carbon content of ~90 wt% and low heteroatom content, *i.e.*, hydrogen and oxygen amount, compared to C-DAP, C-BA, C-HA, and C-DAH. C 1s XPS were collected for 2D nanocarbons (Fig. 3a–g), in which five peaks denoting sp^2 hybridized carbon, sp^3 hybridized carbon, C–O, O–C=O, and HO–C=O were deconvoluted with increasing binding energies.^{39–42} C-EA, C-EDA, and C-PA consist of more than 70% sp^2 -hybridized graphitic domains, less than 15% sp^3 carbon, and a small amount of C–O, O–C=O, and HO–C=O functional groups (Table S2). In this case, the cross-linking between neighbouring sp^2 graphene sheets for these samples is much weaker. The structure thus tends to be more compact and the sp^2 graphene sheets

have a strong tendency to stack into an almost parallel orientation, resulting in uniform slit-like micropores.^{41–45} In contrast, C-DAP, C-BA, C-HA, and C-DAH with large amounts of sp^3 carbon and heteroatoms give rise to a multimodal distribution of micropores. These phenomena are consistent with our previous report.³³

X-ray diffraction (XRD) patterns and Raman spectra were also collected from three representative 2D porous nanocarbons C-EDA, C-PA, and C-DAH to further investigate the effect of the aliphatic chain length of primary amines on the graphitization degree of their carbon products. The thickness and average width of the carbon crystallites, L_c and L_a , were calculated by XRD based on the well-known Scherrer equation, using the FWHM values of (002) at $2\theta = 23^\circ$ and (100) at $2\theta = 43^\circ$ (Fig. 3h). Raman spectroscopy analysis was employed to investigate the degree of graphitic ordering in the carbons (Fig. 3i). The larger L_a and smaller L_c of carbon crystallites and the higher integral intensity ratio of $I_G : I_D$ (G-band and D-band) for C-EDA and C-PA (Table S3†) also indicate that the decrease of the aliphatic chain length of primary amines facilitates the growth of carbon crystallites, and consequently single-sized ultramicropores. The above characterization results provide some insight into the role of primary amines in the formation of the pore structure of 2D nanocarbons. As reported, the lower the carbon number of alkyl chains in primary amines, the stronger the hydrogen bonding strength of the polybenzoxazine network will be,⁴⁶ which results in the higher thermal stability of the formed polybenzoxazine.⁴⁷ After pyrolysis, such carbon counterparts exhibited high carbon content and a large proportion of sp^2 carbon, consequently favouring the formation of unimodal ultramicropores.

Besides uniform pore size, adsorbents with high pore volumes are desirable in order to achieve a large adsorption space. In this work, C-PA with unimodal ultramicropores was activated with K_2CO_3 , which is denoted as C-PA-KC (Fig. 1g, h, and S3†). The surface area and pore volume of the activated sample increase from 463 to 815 $m^2 g^{-1}$ and from 0.26 to 0.41 $cm^3 g^{-1}$, respectively. The proportion of microporosity is 95% of surface area and 88% of pore volume. The pore size of C-PA-KC is uniformly concentrated at 5.6 Å. It is well established that the adsorption potential is maximized for the micropore size of carbonaceous adsorbents, which is ~2 times as large as the kinetic diameter of CO_2 ,^{48–50} resulting in high CO_2 adsorption potential in C-PA-KC. When evaluated as an adsorbent for

Table 1 The synthesis conditions and textural parameters of the prepared 2D porous nanocarbons

Sample	Primary amine	Chemical formula of the primary amine	Pore size (Å)	S_{BET} ($m^2 g^{-1}$)	S_{mic} ($m^2 g^{-1}$)	V_{total} ($cm^3 g^{-1}$)	V_{mic} ($cm^3 g^{-1}$)
C-EA	EA	$CH_3CH_2NH_2$	5.8 ^a	500	480	0.27	0.22
C-EDA	EDA	$NH_2(CH_2)_2NH_2$	5.3	525	510	0.28	0.25
C-PA	PA	$CH_3(CH_2)_2NH_2$	5.8	463	428	0.26	0.23
C-DPA	DAP	$NH_2(CH_2)_3NH_2$	5.8/8.0	493	469	0.27	0.24
C-BA	BA	$CH_3(CH_2)_3NH_2$	5.8/8.0/11.5	542	500	0.30	0.24
C-HA	HA	$CH_3(CH_2)_5NH_2$	5.8/8.0	480	463	0.28	0.25
C-DAH	DAH	$NH_2(CH_2)_6NH_2$	5.8/8.0/11.5	361	309	0.22	0.19

^a Pore size distribution of C-EA has a sharp peak at 5.8 Å.

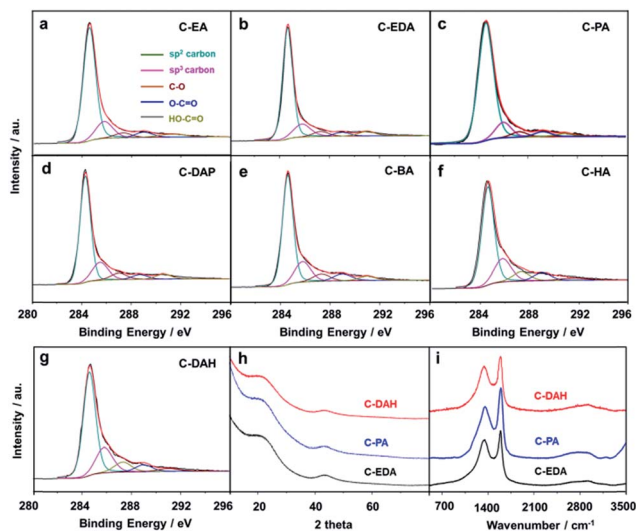


Fig. 3 (a–g) C 1s XPS of 2D porous carbon samples, (h) XRD patterns and (i) Raman spectra of C-EDA, C-PA, and C-DAH.

the capture of CO₂, C-PA-KC can rapidly adsorb CO₂ at very low pressure (≤ 0.15 bar), and the uptakes can reach 5.2 and 7.0 mmol g⁻¹ at 298 K and 273 K and 1 bar, respectively (Fig. 4a). These uptakes are much higher than those of porous carbon materials with similar surface areas reported in the literature, which are attributed to the single-sized ultramicropores that strengthen the host-guest van der Waals interactions. Comparatively, the maximum N₂ uptake of C-PA-KC at 298 K and 1 bar is only 0.3 mmol g⁻¹. The separation selectivity was calculated for C-PA-KC using ideal adsorbed solution theory (IAST), which is 192 for CO₂/N₂ (16/84 v/v%) systems (Fig. 4b). The initial isosteric heat of adsorption for C-PA-KC is 32 kJ mol⁻¹ at low CO₂ uptake based on a variant of the Clausius–Clapeyron equation (Fig. 4c). The low Q_{st} value of CO₂ adsorption on the C-PA-KC characterizes the weak interactions between CO₂ and the 2D nanocarbons, thereby resulting in a relatively simple desorption process and fast adsorption/desorption rates.

The dynamic “breakthrough” separation experiments were conducted in a packed column bed of C-PA-KC at 298 K and 1 bar, using CO₂/N₂ (16/84 v/v%) streams which approximately mimic a flue gas. The “breakthrough curve” demonstrates high separation of CO₂ (Fig. 4d). More specifically, in the mass-transfer zone between the breakthrough point and saturation, the breakthrough curve of CO₂ is much steeper, suggesting a tiny mass-transfer resistance under these conditions, *i.e.*, fast gas diffusion in the C-PA-KC body.⁵¹ The calculated CO₂ mass capacity of C-PA-KC is about 1.6 mmol g⁻¹, which is close to the equilibrium uptakes of single component CO₂ adsorption (1.7 mmol g⁻¹) at a CO₂ partial pressure of 0.16 bar. These dynamic data strongly highlight C-PA-KC with fast adsorption kinetics, high selectivity and high adsorption capacity. Successive regeneration experiments showed that C-PA-KC retained >98% of its intrinsic capacity after mild regeneration (Fig. 4e). The separation efficacy of C-PA-KC under humid conditions was tested by using a gas mixture of CO₂/N₂/H₂O (16/81/3 v/v/v%). The presence of moisture does not affect the separation

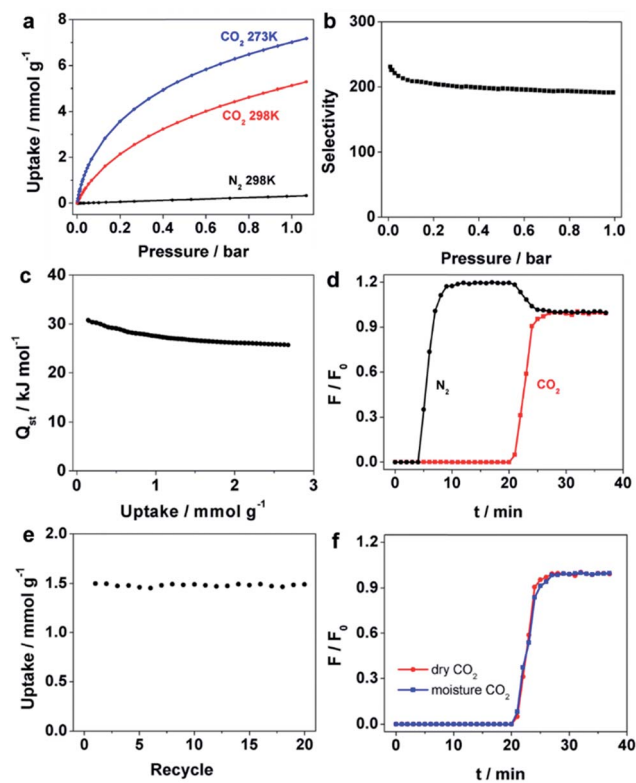


Fig. 4 (a) CO₂ and N₂ adsorption isotherms, (b) IAST selectivity, (c) isosteric heat of adsorption of CO₂, (d) breakthrough curves, (e) cyclic experiments, (f) breakthrough curves in moisture for C-PA-KC.

capability of C-PA-KC, indicating its extraordinary moisture resistance (Fig. 4f). In addition, the sample C-DAH-KC also shows high adsorption capacity (5.0 mmol g⁻¹) and good separation selectivity (162 for CO₂/N₂ (16/84 v/v%)) at 298 K and 1 bar, demonstrating the contribution of the uniform ultramicropores to the gas separation performance (Fig. S4 and S5[†]).

Conclusions

In this study, the influence of the aliphatic chain length of the primary amine moieties on the morphology and micropore structure of 2D polybenzoxazine-based porous nanocarbons was investigated. The shorter the length of aliphatic chains in the amine moieties, the higher the unimodality in micropore size achieved. Our study may provide an efficient and flexible molecular design strategy for precise control of the micropore size distribution in porous carbons. These 2D nanocarbons with single-sized ultramicropores show high separation potential for molecules with similar size and polarizability, such as olefin/paraffin, alkane and aromatic hydrocarbon isomers. Further studies will be carried out along this direction in our laboratory.

Experimental

Chemicals

Resorcinol, ethylamine, ethylenediamine, propylamine, 1,3-diaminopropane, butylamine, hexylamine, 1,6-diaminohexane,

ammonia solution (25 wt%), potassium carbonate (K_2CO_3), hydrochloric acid (HCl) (37 wt%), stearic acid, and formaldehyde (37 wt%) were purchased from Sinopharm Chemical Reagent Co., Ltd. Pluronic F127 was purchased from Sigma. All chemicals were used as received.

Preparation of 2D nanocarbons

2D polybenzoxazine-based nanocarbons were prepared according to a method described in our previous publication.³³ Typically, resorcinol (2 mmol) and formaldehyde (37 wt%) (4 mmol) were first dissolved in water (390 mL) at 28 °C, and then a suspension of stearic acid sheets (10 mL) was added under slow stirring. After the addition of a primary amine (0.25 mmol), the solution became a white suspension within 0.5 h. Ammonia solution (1.5 M) (1 mL) was added to the suspension. The resulting suspension was further heated to 80 °C for another 4 h. Then, the polymer product was washed three times with water, followed by freeze drying. Finally, 2D porous nanocarbons were obtained by pyrolysis of the polymer at 600 °C for 2 h under an argon atmosphere. For the synthesis of C-X-KC, C-X and K_2CO_3 were mixed with a mass ratio of 1 : 2, and then thermal treated at 700 °C for 3 h under an argon atmosphere. The obtained products were washed with HCl (0.2 M) and water until the filtrates became neutral.

Characterization

SEM images were obtained with a FEI NOVA NanoSEM 450 instrument. TEM investigations were carried out with a Tecnai G2 20S-Twin electron microscope equipped with a cold field emission gun. The acceleration voltage was 200 kV. Nitrogen adsorption isotherms were measured with an ASAP 2020 sorption analyzer (Micromeritics) at 77 K. Before the measurements, all the samples were degassed at 200 °C for 4 h. The surface areas (S_{BET}) were calculated using the Brunauer–Emmett–Teller (BET) method. Micropore volumes (V_{mic}) were calculated using the t -plot method. Micropore size distributions (PSDs) were determined based on non-local density functional theory. XPS analysis was carried out with a Thermo VG ESCALAB 250 Microprobe instrument using Al $K\alpha$ radiation as the X-ray source. The binding energy (BE) of the element was calibrated using a C 1s photoelectron peak at 284.6 eV. XRD measurements were performed on an X'Pert-3 Powder diffractometer, using Cu $K\alpha$ radiation ($\lambda = 0.15406$ nm). Raman spectra were recorded on a DXR Microscope Raman Spectrometer, using a 532 nm line of KIMMON laser.

CO₂ sorption and separation measurements

The equilibrium gas uptakes were measured on a Micromeritics ASAP 2020 static volumetric analyzer at a pre-set temperature. Prior to each adsorption experiment, the sample was degassed for 4 h at 200 °C, ensuring that the residual pressure fell below 0.05 mbar, followed by introduction of a single-component gas. For dynamic gas-separation measurements, the separation of CO₂/N₂ (16/84 v/v%) mixtures was performed on a fixed-bed adsorber (a stainless-steel tube with an inner diameter of 8 mm and a length of 130 mm) at 1 bar and 298 K. The mass of

the adsorbent is 1.434 g. First, the bed was heated at 50 °C in Ar at a flow rate of 50 mL min⁻¹ for 2 h. Then, the breakthrough experiments were conducted by abruptly switching from Ar to the gas mixture with a total flow rate of 12 mL min⁻¹. A sample saturated with gas molecules was subjected to an Ar flow of 15 mL min⁻¹ under ambient conditions. After 30 min, no gas molecule was detected in the effluent. The effluent gas was monitored online by using an Agilent 7890A gas chromatograph with a thermal conductivity detector (TCD).

The (absolute) adsorbed amount is calculated from breakthrough curve using the equation:

$$q_i = \frac{F_0 \times t_0 - V_{dead} - \int_0^{t_0} F_i \Delta t}{m}$$

where F_0 is the total volumetric gas flow rate; t_0 is the adsorption time (min); V_{dead} is the dead volume of the column and line; F_i is effluent volumetric flow rate; m is the mass of the adsorbent.

Conflicts of interest

There are no conflicts to declare.

Acknowledgements

The authors are grateful for the financial support from the National Natural Science Foundation of China (No. 21473021 and No. 21776041), and Cheung Kong Scholars Program of China (T2015036).

Notes and references

- Z. Y. Jin, Y. Y. Xu, Q. Sun and A. H. Lu, *Small*, 2015, **11**, 5151–5156.
- Y. Fang, Y. Lv, R. Che, H. Wu, X. Zhang, D. Gu, G. Zheng and D. Zhao, *J. Am. Chem. Soc.*, 2013, **135**, 1524–1530.
- G.-P. Hao, A.-H. Lu, W. Dong, Z.-Y. Jin, X.-Q. Zhang, J.-T. Zhang and W.-C. Li, *Adv. Energy Mater.*, 2013, **3**, 1421–1427.
- X. Zheng, J. Luo, W. Lv, D. W. Wang and Q. H. Yang, *Adv. Mater.*, 2015, **27**, 5388–5395.
- H. Fan and W. Shen, *ChemSusChem*, 2015, **8**, 2004–2027.
- Y. Dong, M. Yu, Z. Wang, Y. Liu, X. Wang, Z. Zhao and J. Qiu, *Adv. Funct. Mater.*, 2016, **26**, 7590–7598.
- R. Sakamoto, K. Hoshiko, Q. Liu, T. Yagi, T. Nagayama, S. Kusaka, M. Tsuchiya, Y. Kitagawa, W. Y. Wong and H. Nishihara, *Nat. Commun.*, 2015, **6**, 6713–6721.
- X. Xiao, H. Song, S. Lin, Y. Zhou, X. Zhan, Z. Hu, Q. Zhang, J. Sun, B. Yang, T. Li, L. Jiao, J. Zhou, J. Tang and Y. Gogotsi, *Nat. Commun.*, 2016, **7**, 11296–11303.
- Z. Sun, T. Liao, Y. Dou, S. M. Hwang, M. S. Park, L. Jiang, J. H. Kim and S. X. Dou, *Nat. Commun.*, 2014, **5**, 3813–3821.
- T. Rodenas, I. Luz, G. Prieto, B. Seoane, H. Miro, A. Corma, F. Kapteijn, I. X. F. X. Llabres and J. Gascon, *Nat. Mater.*, 2015, **14**, 48–55.
- G.-P. Hao, Z.-Y. Jin, Q. Sun, X.-Q. Zhang, J.-T. Zhang and A.-H. Lu, *Energy Environ. Sci.*, 2013, **6**, 3740–3747.

- 12 S. Wang, F. Cheng, P. Zhang, W.-C. Li and A.-H. Lu, *Nano Res.*, 2017, **10**, 2106–2116.
- 13 Z. Y. Jin, A. H. Lu, Y. Y. Xu, J. T. Zhang and W. C. Li, *Adv. Mater.*, 2014, **26**, 3700–3705.
- 14 X. Wang, L. L. Lu, Z. L. Yu, X. W. Xu, Y. R. Zheng and S. H. Yu, *Angew. Chem., Int. Ed.*, 2015, **54**, 2397–2401.
- 15 Z. S. Wu, Y. Sun, Y. Z. Tan, S. Yang, X. Feng and K. Mullen, *J. Am. Chem. Soc.*, 2012, **134**, 19532–19535.
- 16 L. Shang, T. Bian, B. Zhang, D. Zhang, L. Z. Wu, C. H. Tung, Y. Yin and T. Zhang, *Angew. Chem., Int. Ed.*, 2014, **53**, 250–254.
- 17 S. Yang, X. Feng, L. Wang, K. Tang, J. Maier and K. Mullen, *Angew. Chem., Int. Ed.*, 2010, **49**, 4795–4799.
- 18 D. Krishnan, K. Raidongia, J. Shao and J. Huang, *ACS Nano*, 2014, **8**, 449–457.
- 19 R. Li, Z. Wei and X. Gou, *ACS Catal.*, 2015, **5**, 4133–4142.
- 20 B. Jang, M. Park, O. B. Chae, S. Park, Y. Kim, S. M. Oh, Y. Piao and T. Hyeon, *J. Am. Chem. Soc.*, 2012, **134**, 15010–15015.
- 21 X. Liu and M. Antonietti, *Adv. Mater.*, 2013, **25**, 6284–6290.
- 22 S. H. Yu, D. J. Lee, M. Park, S. G. Kwon, H. S. Lee, A. Jin, K. S. Lee, J. E. Lee, M. H. Oh, K. Kang, Y. E. Sung and T. Hyeon, *J. Am. Chem. Soc.*, 2015, **137**, 11954–11961.
- 23 L. Wang, S. Dou, J. Xu, H. K. Liu, S. Wang, J. Ma and S. X. Dou, *Chem. Commun.*, 2015, **51**, 11791–11794.
- 24 D. Y. Chung, M. J. Kim, N. Kang, J. M. Yoo, H. Shin, O.-H. Kim and Y.-E. Sung, *Chem. Mater.*, 2017, **29**, 2890–2898.
- 25 Z. Fan, Y. Liu, J. Yan, G. Ning, Q. Wang, T. Wei, L. Zhi and F. Wei, *Adv. Energy Mater.*, 2012, **2**, 419–424.
- 26 Z. Li, M. Shao, L. Zhou, R. Zhang, C. Zhang, M. Wei, D. G. Evans and X. Duan, *Adv. Mater.*, 2016, **28**, 2337–2344.
- 27 S. Schrettl, C. Stefanu, C. Schwieger, G. Pasche, E. Oveisi, Y. Fontana, A. Fontcuberta i Morral, J. Reguera, R. Petraglia, C. Corminboeuf, G. Brezesinski and H. Frauenrath, *Nat. Chem.*, 2014, **6**, 468–476.
- 28 J. Hou, C. Cao, F. Idrees and X. Ma, *ACS Nano*, 2015, **9**, 2556–2564.
- 29 J. Xu, J. Zhu, X. Yang, S. Cao, J. Yu, M. Shalom and M. Antonietti, *Adv. Mater.*, 2016, **28**, 6727–6733.
- 30 S. Wang, W. C. Li, G. P. Hao, Y. Hao, Q. Sun, X. Q. Zhang and A. H. Lu, *J. Am. Chem. Soc.*, 2011, **133**, 15304.
- 31 S. Wang, W.-C. Li, L. Zhang, Z.-Y. Jin and A.-H. Lu, *J. Mater. Chem. A*, 2014, **2**, 4406–4412.
- 32 G. P. Hao, W. C. Li, D. Qian, G. H. Wang, W. P. Zhang, T. Zhang, A. Q. Wang, F. Schuth, H. J. Bongard and A. H. Lu, *J. Am. Chem. Soc.*, 2011, **133**, 11378–11388.
- 33 L. H. Zhang, W. C. Li, H. Liu, Q. G. Wang, L. Tang, Q. T. Hu, W. J. Xu, W. H. Qiao, Z. Y. Lu and A. H. Lu, *Angew. Chem., Int. Ed.*, 2018, **57**, 1632–1635.
- 34 A. Arnebold, O. Schorsch, J. Stelten and A. Hartwig, *J. Polym. Sci., Part A: Polym. Chem.*, 2014, **52**, 1693–1699.
- 35 G. P. Hao and A. H. Lu, *Advanced and Emerging Polybenzoxazine Science and Technology*, 2017, ch. 32, pp. 621–642.
- 36 Q. Ran, Y. Gu and H. Ishida, *Advanced and Emerging Polybenzoxazine Science and Technology*, 2017, ch. 11, pp. 171–204.
- 37 K. Hemvichiana, A. Laobutheeb, S. Chirachanchaib and H. Ishida, *Polym. Degrad. Stab.*, 2002, **71**, 1–15.
- 38 H. Ishida and T. Agag, *Handbook of Benzoxazine Resins*, Elsevier, 2011.
- 39 B. Zhang, C. M. Ghimbeu, C. Laberty, C. Vix-Guterl and J.-M. Tarascon, *Adv. Energy Mater.*, 2016, **6**, 1501588–1501596.
- 40 L. Zhang, X. Yang, F. Zhang, G. Long, T. Zhang, K. Leng, Y. Zhang, Y. Huang, Y. Ma, M. Zhang and Y. Chen, *J. Am. Chem. Soc.*, 2013, **135**, 5921–5929.
- 41 Z. L. Yu, S. Xin, Y. You, L. Yu, Y. Lin, D. W. Xu, C. Qiao, Z. H. Huang, N. Yang, S. H. Yu and J. B. Goodenough, *J. Am. Chem. Soc.*, 2016, **138**, 14915–14922.
- 42 H. Richter, H. Voss, N. Kaltenborn, S. Kamnitz, A. Wollbrink, A. Feldhoff, J. Caro, S. Roitsch and I. Voigt, *Angew. Chem., Int. Ed.*, 2017, **56**, 7760–7763.
- 43 R. E. Franklin, *Proc. R. Soc. London, Ser. A*, 1951, **209**, 196–218.
- 44 M. Rungta, G. B. Wenz, C. Zhang, L. Xu, W. Qiu, J. S. Adams and W. J. Koros, *Carbon*, 2017, **115**, 237–248.
- 45 C. Zhang and W. J. Koros, *Adv. Mater.*, 2017, **29**, 1701631–1701636.
- 46 H. Ishida and H. Y. Low, *Macromolecules*, 1997, **30**, 1099–1106.
- 47 H. Y. Low and H. Ishida, *J. Polym. Sci., Part B: Polym. Phys.*, 1998, **36**, 1935–1946.
- 48 V. Presser, J. McDonough, S.-H. Yeon and Y. Gogotsi, *Energy Environ. Sci.*, 2011, **4**, 3059–3066.
- 49 J. W. To, J. He, J. Mei, R. Haghpanah, Z. Chen, T. Kurosawa, S. Chen, W. G. Bae, L. Pan, J. B. Tok, J. Wilcox and Z. Bao, *J. Am. Chem. Soc.*, 2016, **138**, 1001–1009.
- 50 D. Qian, C. Lei, E. M. Wang, W. C. Li and A. H. Lu, *ChemSusChem*, 2014, **7**, 291–298.
- 51 H. He, L. Zhuang, S. Chen, H. Liu and Q. Li, *Green Chem.*, 2016, **18**, 5859–5869.